J. Fluid Mech. (2024), *vol.* 997, A15, doi:10.1017/jfm.2024.766

Mass transfer during drop impact on a thin film

Muhammad Osama[1], **Robert D. Deegan**[2],† **and G. Gilou Agbaglah**[1],†

[1]Department of Mechanical Engineering, Wayne State University, Detroit, MI 48202, USA
[2]Department of Physics, University of Michigan, Ann Arbor, MI 48109, USA

(Received 4 April 2024; revised 14 August 2024; accepted 14 August 2024)

We conducted an axisymmetric numerical study of drop impact on a thin film of the same liquid in order to generate maps identifying the fluid elements in the drop and film that are transferred to the corolla during impact. We find that mass contribution from the drop comes from a surprisingly thin surface layer on the drop, and furthermore, that the shape of this layer in the drop and the film scales with film thickness, not the Weber number and Reynolds number as one might expect. The maps could be used to tailor drop composition for applications such as coatings or encapsulations.

Key words: breakup/coalescence

1. Introduction

Drop impact is pivotal in a wide range of fluid applications such as printing (Lohse 2022), hydrophobic coatings (Gauthier *et al.* 2015), ice formation on aeroplanes (Khojasteh *et al.* 2016), disease spread (Bourouiba 2021), cooling (Breitenbach, Roisman & Tropea 2018; Aksoy *et al.* 2021), atomized sprays (Villermaux 2007; Moreira, Moita & Panao 2010), and microphysics processes in clouds and aerosols (Carslaw *et al.* 2013), to name a few. Splashing from drop impact is defined as the generation of additional smaller droplets following the initial impact, called secondary droplets. One of the outstanding challenges in drop impact research is understanding the various processes affecting the characteristics of secondary droplets (Liang & Mudawar 2016).

The focus here is on the transfer of mass during the impact of a drop with a film that is much thinner than the drop's diameter. When a drop impact event is sufficiently energetic, sheet-like jets form that typically are axisymmetric at onset but may later break symmetry and fragment into secondary droplets. Multiple distinct jets have been identified, distinguished by the time scale at which they emerge, their formation mechanism, and their

---

† Email addresses for correspondence: rddeegan@umich.edu, gilou.agbaglah@wayne.edu

characteristics (Yarin 2006). The so-called ejecta jet (Weiss & Yarin 1999; Thoroddsen 2002) emerges within tens of microseconds after impact, displays speeds many times that of the drop, and is thought to be produced by an overpressure condition (Weiss & Yarin 1999; Davidson 2002; Howison *et al.* 2005). A single impact event may produce several generations of ejecta jets (Zhang *et al.* 2012). The so-called corolla (sometimes called the lamella, crown, corona or Peregrine sheet) emerges on the time scale commensurate with the merger time of the drop and film (approximately 1 ms); its speed is close to the drop speed, and it is thought to be produced by a collision of the liquid from the drop with that of the film (Peregrine 1981; Yarin & Weiss 1995), causing an upward deflection of the combined fluid that leads to an axisymmetric sheet-like jet as shown in figure 4. As the corolla grows, its leading edge destabilizes and ultimately fragments into secondary droplets. Whereas ejectas and corollas are sheet-like jets resulting from the impact, another jet characterized by its spike-like shape, called the Worthington jet, forms from the collapse of the cavity in the film produced by the impact event. Whether a particular jet manifests depends on the fluid and kinematic parameters. We restricted our simulation to events in which the corolla is the only jet that forms.

Due to its importance in practical applications, drop impact has been studied extensively, revealing the phenomenology of splashing (Worthington & Cole 1897; Rein 1993; Xu 2007; Deegan, Brunet & Eggers 2008), and its dependence on multitudinous experimental conditions such as temperature (e.g. Aziz & Chandra 2000; Tran *et al.* 2012; Liang & Mudawar 2017), surface preparation (e.g. Marengo *et al.* 2011; Josserand & Thoroddsen 2016), additives (e.g. Aksoy *et al.* 2021), incidence angle, tangential speed (e.g. Castrejón-Pita *et al.* 2016), and many more (Liang & Mudawar 2016). By comparison, the question about what parts of the drop and film contribute to a splash has received less attention (for exceptions, see e.g. Stumpf *et al.* 2022; Fudge *et al.* 2023; Stumpf *et al.* 2023). Answering this question may lead to new techniques for controlling environmental transport phenomena, encapsulation and coating technology.

In this paper, we identify the fluid elements in the drop and film that are transferred to the corolla at different times. Investigating this transfer experimentally is challenging (see e.g. Stumpf *et al.* 2022), so instead we use high-resolution two-phase numerical axisymmetric simulations for multiple Reynolds and Weber numbers and film thicknesses. The imposition of axisymmetry is consistent with the experimental observation that corollas are typically axisymmetric at early times. We find a number of remarkable features: the mass of fluid in the drop that ultimately enters the corolla is confined to a thin surface layer, and most surprisingly its characteristic dimensions are almost entirely determined by the thickness of the film rather than by a combination of Weber and Reynolds numbers, as one might expect based on extensive prior work characterizing splashing (see e.g. Mundo, Sommerfeld & Tropea 1995; Rioboo *et al.* 2003; Josserand & Zaleski 2003; Deegan *et al.* 2008; van der Veen *et al.* 2012).

In § 2, we present our numerical methods, the simulation configuration, its validation, and our parameter space, and the post-processing techniques to identify the corolla and to track the fluid elements entering it. In § 3, we present a series of maps showing the domains of fluid elements that will go on to form the corolla at various later times. The most salient features of these maps are the shape and scaling properties of the domains. We show that the shape scales with the depth of the film but is almost independent of the Weber and Reynolds numbers. In § 4, we discuss the various theories proposed for crown formation, and their relevance and applicability to the maps.

2. Methods

2.1. *Numerical method*

Numerical treatments of wet drop impact in two and three dimensions have been developed extensively. Harlow & Shannon (1967) conducted some of the first numerical computations using an axisymmetric code that neglected surface tension. Weiss & Yarin (1999), and later Davidson (2002), used the boundary integral method on an axisymmetric domain and an inviscid formulation of the dynamics to show the existence of a jet preceding the corolla, the so-called ejecta jet. Rieber & Frohn (1999) were the first to perform fully three-dimensional computations using a volume-of-fluid method, and argued that the instability of the corolla is due to the Rayleigh instability. Currently, drop impact simulations can be performed routinely and reliably using open source software such as Gerris and Basilisk (Thoraval *et al.* 2012; Agbaglah & Deegan 2014; Josserand, Ray & Zaleski 2016), particularly when supplemented by experimental results as we do here. Axisymmetric computations are readily realized on reasonably sized clusters. While in principle fully three-dimensional computations are possible, they continue to strain resources, and the issues of numerical artefacts arising from changes in topology are not fully resolved (see e.g. Afanador *et al.* 2021; Zhou *et al.* 2021).

We model a gas–liquid system with the incompressible Navier–Stokes equation, utilizing the one-fluid approach:

$$\rho(\partial_t \boldsymbol{u} + \boldsymbol{u}\cdot\nabla\boldsymbol{u}) = -\nabla p + \nabla\cdot(2\mu\boldsymbol{D}) + \gamma\kappa\delta_s\boldsymbol{n}, \tag{2.1}$$

$$\nabla\cdot\boldsymbol{u} = 0, \tag{2.2}$$

where $\boldsymbol{u}$ is the velocity of the fluid, $\mu \equiv \mu(\boldsymbol{x}, t)$ is the viscosity, $\rho \equiv \rho(\boldsymbol{x}, t)$ is the density, and $\boldsymbol{D}$ is the deformation tensor. The densities and viscosities are constant in each phase, with values ρ_g and μ_g in the gas, and ρ_l and μ_l in the fluid. The surface tension term acts only at the interface and is included in (2.1) by a Dirac function δ_s, with prefactors κ and $\boldsymbol{n}$ denoting the local curvature and normal unit vector to the interface, respectively.

We use the Basilisk open-source solver (Popinet 2018), which is an enhanced version of the Gerris solver widely used for various multiphase flow problems (Agbaglah *et al.* 2011, 2015; Thoraval *et al.* 2012; tao Li *et al.* 2014; Visser *et al.* 2015; Ling *et al.* 2016; Osama *et al.* 2022). In Basilisk, the liquid–gas interface is tracked by the volume-of-fluid method on an octree structured grid facilitated by adaptive mesh refinement. The adaptive mesh refinement in this study relies on a criterion of wavelet-estimated discretization error (Van Hooft *et al.* 2018). To define physical properties such as μ and ρ, the volume fraction of the liquid phase f is utilized to linearly interpolate these quantities in cells containing the liquid–gas interface:

$$\mu(f) = f\mu_l + (1-f)\mu_g, \tag{2.3}$$

$$\rho(f) = f\rho_l + (1-f)\rho_g. \tag{2.4}$$

The transport equation of f is computed from

$$\partial_t f + \nabla\cdot(\boldsymbol{u}f) = 0. \tag{2.5}$$

Basilisk uses a balanced-force technique to calculate the surface tension, and the interface's curvature is determined using the height function approach. Further elaboration on the numerical methods utilized in Basilisk can be found in Popinet (2003, 2009).

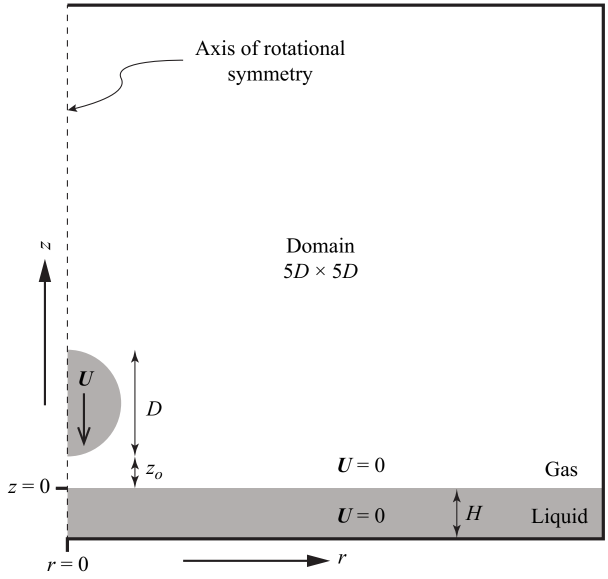

Figure 1. A spherical drop of diameter D falls vertically through a gas with speed U and collides with a film of thickness H of the same liquid. Initially, the velocity is zero everywhere except in the drop, and the drop is at a vertical distance $z_o = 10^{-3}D$ above the film surface. The simulations were performed on an axisymmetric domain $5D \times 5D$, with the dashed line as the axis of symmetry. No-slip boundary conditions were enforced on the other three boundaries.

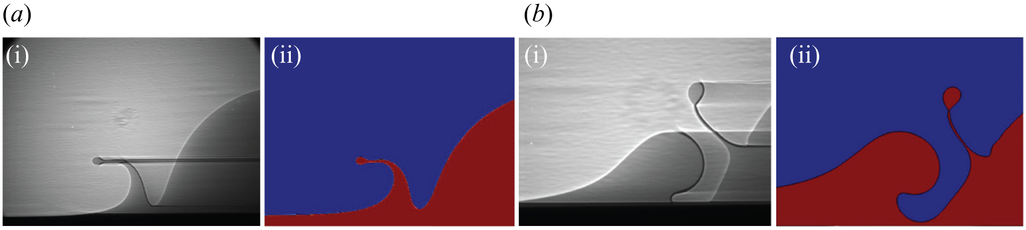

Figure 2. Comparison of X-ray images of drop impact on a deep pool (greyscale images) and the corresponding snapshot from numerical simulations with the same dimensionless parameters: (*a* i,ii) $We = 324$, $Re = 2191$; (*b* i,ii) $We = 451$, $Re = 710$. Adapted from Agbaglah & Deegan (2014).

2.2. *Numerical simulations*

We modelled a spherical drop with initial diameter D and velocity U impacting a film of the same liquid with thickness H as shown in figure 1. The computational domain was $5D \times 5D$ in size, and axially symmetric with the axis of symmetry along the vertical centreline of the drop. No-slip boundary conditions were enforced on the top, bottom and right-hand edges of the domain. The grid was discretized using adaptive mesh refinement with minimum spacing $5D/2^{14}$ along each dimension. This level of refinement corresponds to a minimum mesh size $\Delta x = D/3277$, and was shown previously to accurately represent experimental results (Agbaglah & Deegan 2014) as shown in figure 2. The simulations were initialized with the drop's bottom at a vertical distance $0.001D$ above the film's upper surface, and with a velocity field equal to $-U\boldsymbol{z}$ within the drop, and zero everywhere else.

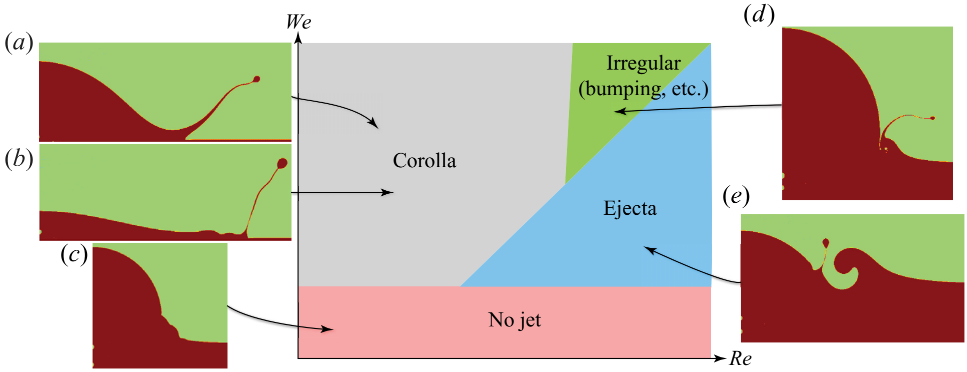

Figure 3. Qualitative phase diagram for the type of splash observed. The boundaries vary with depth, but the overall structure remains the same (Cossali, Coghe & Marengo 1997; Rioboo *et al.* 2003; Thoraval *et al.* 2012; Agbaglah *et al.* 2015). Our simulations focus on impact events that produce only a corolla as in (*a*) $Re = 1000$, $We = 500$, $h = 0.025$, $t = 0.6$ and (*b*) $Re = 2042$, $We = 292$, $h = 0.025$, $t = 1.05$. The flows outside of the corolla regime are (*c*) $Re = 2000$, $We = 100$, $h = 0.2$, $t = 0.3$, (*d*) $Re = 3000$, $We = 500$, $h = 0.2$, $t = 0.3$, (*e*) $Re = 2042$, $We = 292$, $h = 0.4$, $t = 0.7$.

The system is characterized by five dimensionless groups: the Reynolds number $Re = \rho_l UD/\mu_l$, the Weber number $We = \rho_l U^2 D/\sigma$, the dimensionless thickness $h \equiv H/D$, and the ratios of the liquid and gas dynamic viscosity $\varLambda = \mu_l/\mu_g$ and density ρ_l/ρ_g. We fixed the values of $D = 0.2\,\text{cm}$, $U = 190\,\text{cm}\,\text{s}^{-1}$, $\rho_l = 0.851\,\text{g}\,\text{cm}^{-3}$, $\rho_g = 1.293 \times 10^{-3}\,\text{g}\,\text{cm}^{-3}$, $\mu_g = 1.90 \times 10^{-2}\,\text{cP}$, and varied μ_l, σ and H to tune the values of Re, We and h, respectively. All results below are reported in dimensionless units, where lengths are scaled by D and times by D/U.

The ranges of values for the Weber number, Reynolds number and dimensionless thickness in our study were chosen to focus exclusively on impact events that produce a corolla without a separate ejecta – i.e. events such as in figure 2(*a*) rather than figure 2(*b*) – while remaining close to $Re = 2191$, $We = 324$ where we can validate our simulations. The constraints are illustrated schematically in figure 3 in the Re–We plane; the boundaries depicted therein shift with depth.

Higher values of h combined with low We and high Re tend to produce a separate ejecta; we observed, for example, that at $h = 0.4$ for $Re = 2042$ and $We = 292$, an ejecta is present. Thus we limited $h \leq 0.2$. Low values of h are difficult to achieve experimentally (see e.g. Wang & Chen 2000). For example, $h = 0.015$ corresponds to a $30\,\mu\text{m}$ film for a 2 mm drop. Moreover, qualitatively different flows appear after some time at low values of h, such as the one shown in figure 4(*f*). Thus we limited $h \geq 0.015$.

Low Weber numbers are insufficiently energetic to produce a corolla, but too large a value produces a separate ejecta (Agbaglah *et al.* 2015). For example, with $We = 100$, $Re = 1000, 2000, 3000$ and $h = 0.03, 0.05, 0.2$, a corolla does not form. At higher values of the Reynolds and Weber numbers, the corolla begins to interact with the drop (see ‘bumping’ and other phenomena in Thoraval *et al.* 2013). We observed bumping at $Re = 3000$, $We = 500$, $h = 0.2$. Thus we settled on the ranges $500 \geq We \geq 100$ and $3000 \geq Re \geq 1000$.

Since the dependence on the density and viscosity ratios between the gas and liquid is almost insignificant for the range of values in typical experiments, these were not varied

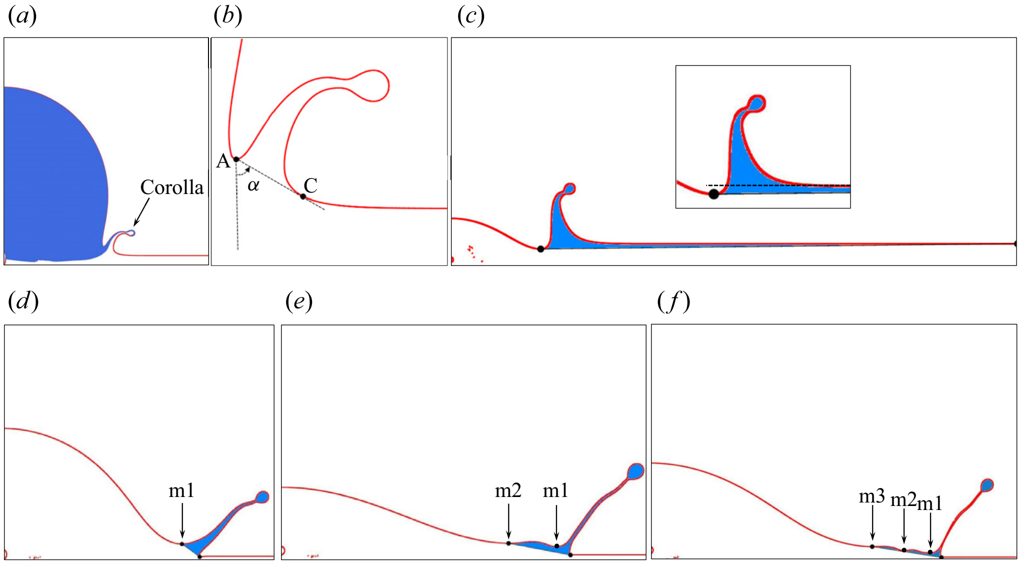

Figure 4. Defining the corolla. (*a*) Simulation with $Re = 1000$, $We = 292$, $h = 0.05$ at $t = 0.2$, with the interface in red, and the fluid originally in the drop and film in blue and white, respectively. (*b*) Magnified view of the corolla, with markers used to define its boundaries. Point A is the local minimum in z of the interface (r, z) nearest $r = 0$. Point C is found by iteratively rotating anticlockwise a vertical line through point A until it meets the interface. (*c–f*) Problematic surface profiles. (*c*) For thick films at late times ($h = 0.2$ at $t = 0.9$ shown), point A falls below the film's initial surface height, and it is no longer possible to construct a tangent. (*d–f*) Surface profiles for $Re = 1000$, $We = 292$, $h = 0.025$ at $t = 0.5, 0.8, 0.995$, illustrating the appearance of multiple minima.

Re	We	h	Λ	ρ_l/ρ_g
500	292	0.025, 0.05, 0.2	260	709
1000	292	0.015, 0.025, 0.035, 0.05, 0.1, 0.2	130	709
1000	500	0.015, 0.025, 0.035, 0.05, 0.1, 0.2	130	709
2000	150	0.025, 0.05	65	709
2042	292	0.015, 0.025, 0.035, 0.05, 0.1, 0.2	64	709
2042	500	0.015, 0.025, 0.035, 0.05, 0.1, 0.2	64	709
3000	292	0.025, 0.05, 0.2	43	709
3000	500	0.025, 0.05	43	709

Table 1. Parameters for numerical simulations.

systematically. The density ratio was fixed at 709 for all simulations, and the viscosity ratio changed with Re.

The parameter values for all 34 simulations are listed in table 1. Each simulation (i.e. a single combination of (Re, We, h)) took approximately two days on 32 cores (1536 CPU hours), using Basilisk's parallelization capabilities and adaptive mesh refinement, and required up to 0.5 TB of storage for the output files. Post-processing to backtrack the fluid elements (see algorithm below) required up to an additional three days on a single core, and 62 GB of random access memory.

The main advantage of an axisymmetric simulation is the modest computational resources needed, when compared to those needed in a three-dimensional domain. The latter would require, using the adaptive mesh refinement, roughly 1.6×10^6 CPU hours and 3 PB of disk space per set of (Re, We). Given the number of simulations and the resources available to us, performing our study in three dimensions was infeasible. A downside of an axisymmetric simulation of drop impact is that it cannot reproduce the longitudinal destabilization of the corolla's edge that ultimately produces secondary droplets. This disadvantage is somewhat mitigated by the well-known difficulties of resolving droplet pinch-off in three dimensions (Afanador *et al.* 2021; Zhou *et al.* 2021), and experiments show that the corolla is approximately axisymmetric for times less than D/U (i.e. $t < 1$) for the parameter range of our study.

2.3. *Defining the corolla*

Physical experiments in the parameter regime of our study (table 1) produce an initially axisymmetric corolla that ultimately breaks up into secondary droplets. The corolla in our simulations appears in cross-section as a thin strip of fluid rising from where the drop and film meet, as shown in figure 4(*a*). Unlike in experiments, corolla break-up is not possible because of the imposed axial symmetry.

Dividing the liquid domain into parts inside and outside the corolla proved challenging since no criteria that we tried based on identifiable features on the interface, velocity or vorticity field worked for all parameters and all times. Ultimately, we adopted the criteria shown in figure 4(*b*), because this worked with the greatest number of simulations. We define point A to be the first minimum of the interface height encounter moving along the interface, starting from the centre of the drop. Next, we found the line segment through point A and tangent to the interface on the other side of the corolla, as shown in figure 4(*b*). Any fluid inside the curve composed of the interface between points A and C and the line segment AC is defined to be in the corolla.

This definition for the boundary of the corolla always works at short times, but breaks down under two different conditions at late times. For thick films, the vertical position of point A decreases and ultimately falls below the undisturbed height of the film (or equivalently, its position at infinity), and thereafter the tangent curve no longer exists (see figure 4*c*). For the thinnest films at late times, multiple minima appear between the drop centre and the corolla's tip, as shown by the sequence in figures 4(*d–f*), so point A fails to be unique. Selecting the first minimum leads to an unappealing definition of the corolla, and switching to the second minimum (say, when it falls below the first) leads to a discontinuity of the mass inside the corolla. Overall, our definition of the corolla's boundary works in approximately 80 % of the parameter–time combinations, which is better than any other definition that we tried.

2.4. *Lagrangian tracking of the fluid elements*

We computed the Lagrangian trajectories of fluid elements from the flow calculation to determine if a particular element is inside or outside the corolla at some particular future time. It proved more accurate to compute the trajectories backwards in time, starting with the elements position in the corolla and tracing its origin back to $t = 0$ (Dubitsky, Mcrae & Bird (2023) employed a similar technique). First, the Basilisk output files were post-processed using Python's shapely.geometry module to identify every mesh point inside the corolla at 0.1 time increments from 0.1 to 0.9. Next, the backwards-in-time trajectory of each mesh point was computed using the time-reversed flow field stored in the output files from Basilisk with time resolution $\delta t \equiv 5 \times 10^{-4}$. The first two time

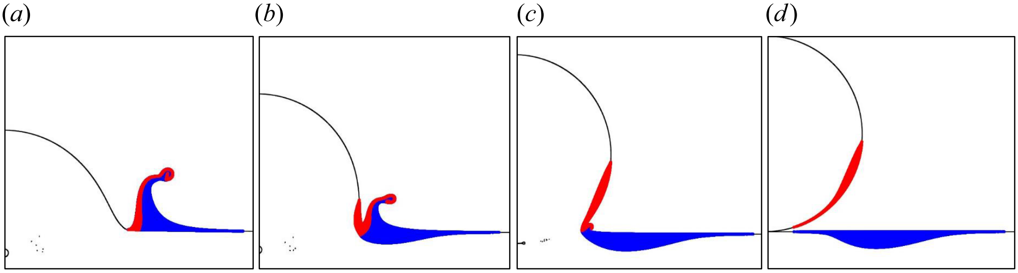

Figure 5. Backtracking. Simulation snapshots for $Re = 1000$, $We = 292$, $h = 0.2$, with the interface shown as a black line, and the tracers placed inside the corolla shown in red and blue at (*a*) $t = 0.5$. (*b–d*) The advection of the tracers at $t = 0.3, 0.1, 0.0$. The tracers are coloured red or blue to indicate their ultimate destination in the drop or the film, respectively.

steps were computed using a first-order Euler method with time-step size δt. These data were then used to initialize a third-order Adams–Bashforth scheme for the subsequent steps, tracing the elements position back to $t = 0$. Thus the trajectory for each mesh point for each of the nine starting times is computed separately. The algorithm applied to one particular start time yields a sequence such as that shown in figure 5. The final frame of this sequence is an example of the main result of our computations: it shows the domain of fluid elements prior to impact that will form the corolla at some later time, $t = 0.5$ in this particular case.

A few trajectories near the liquid–air interface or the computational domain boundary stray across these boundaries. Since this unphysical behaviour is caused by the finite time-step size in our backtracking algorithm and was infrequent, we discarded such trajectories. This elimination scheme was employed most often for the thinnest films, and was most acute for mesh points that begin near the bottom solid boundary. In the most adverse case ($Re = 2042$, $We = 292$, $h = 0.015$), this occurred for approximately 3 % of tracers.

3. Results

We follow the Lagrangian path of fluid elements in the drop or film starting at $t = 0$, and determine if it ends up in the corolla at some particular time $t > 0$. By tracing all such elements, we construct domains of fluid elements that ultimately enter the corolla. These domains at any given time consist of two disjoint subdomains: one for the drop and one for the film, since both contribute to the corolla. Examples of these domains are shown in figure 6, colour-coded to indicate the time when they entered the corolla. We refer to these diagrams as maps since they show which parts of the drop and film will evolve into the corolla.

The main qualitative features of these maps are: (i) the fluid contribution from the drop to the corolla comes from a narrow sliver on the surface of the drop starting near its south pole; (ii) the shapes of the domains in the drop are generally similar in appearance, having a comma-like shape; (iii) the percentage of mass contributed by the film versus the drop changes with film thickness, with the drop contribution dominating for the thinnest films; and (iv) the mass contribution from the film comes from all depths for the thinnest films. Below, we quantify these observations and show that drop domains have a self-similar shape.

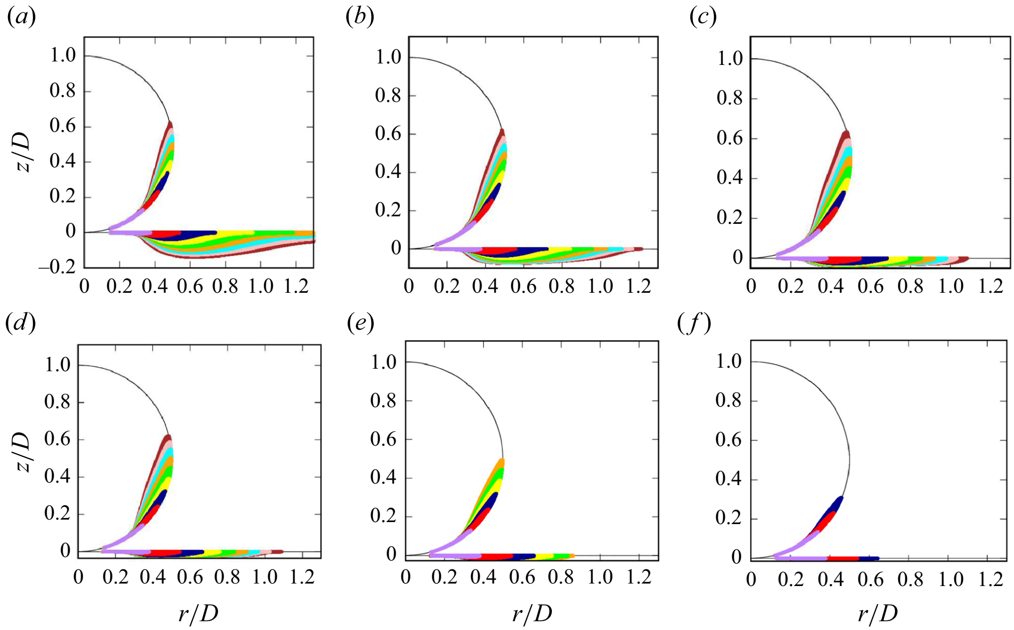

Figure 6. Mass transfer maps for $Re = 1000$, $We = 292$ and h values (*a*) 0.2, (*b*) 0.1, (*c*) 0.05, (*d*) 0.035, (*e*) 0.025, (*f*) 0.015. The colours identify elements that enter the corolla prior to t values 0.1 (purple), 0.2 (red), 0.3 (dark blue), 0.4 (yellow), 0.5 (green), 0.6 (orange), 0.7 (cyan), 0.8 (pink), 0.9 (brown). There are fewer data points in (*e*,*f*) because of the ambiguity in delineating the corolla, as discussed in the text and figure 4.

We characterized the domains by their lengths L_d and L_f, thicknesses W_d and W_f, and volumes V_d and V_f, as illustrated in figure 7. The subscripts denote drop (d) and film (f). In order to measure domains inside the drop, it is convenient to unroll its shape with polar coordinates so that positions (r, z) in the simulation are mapped to $\rho = \sqrt{r^2 + (z_c - z)^2}$ and $\tan\theta = r/(z_c - z)$, where $(0, z_c)$ is the position of the drop's centre at $t = 0$.

Figure 8 shows a plot of the length of the drop domain versus time for all 34 simulations. Surprisingly, there is little variation in the magnitude of this quantity with any of the simulation parameters Re, We, h. The small variation correlates most strongly with h: following any one colour (corresponding to fixed Re and We) in figure 8(*b*) shows a 2–4 % variation, whereas following any one symbol (corresponding to fixed h) in figure 8 shows variation of at most 1 %. Henceforth, we adopt L_d rather than time as a measure of the impact event's progress.

Figure 9(*a*) is a plot of W_d versus L_d that includes all the simulations in our study. Around any fixed value of L_d, or equivalently at a fixed time after impact, W_d shows large variation. As an example, for $L_d \approx 0.6$ shown in the inset of figure 9(*a*), W_d varies by 100–200 %. Figure 9(*c*) plots these variations versus h, We and Re, showing that they are primarily due to h.

The same case can be made for the other parameters, W_f, V_d, V_f, L_f. The lack of sensitivity to We and Re suggests searching for a collapse of the data with a scaling relationship that depends only on h, of the form

$$y = h^{\alpha} f\left(L_d h^{-\beta}\right), \tag{3.1}$$

where $f(\cdot)$ is an arbitrary function (Barenblatt 2003). Such a scaling exists and is shown for W_d in figure 9(*b*), for V_d, W_f, V_f in figure 10, and for L_f in figure 11.

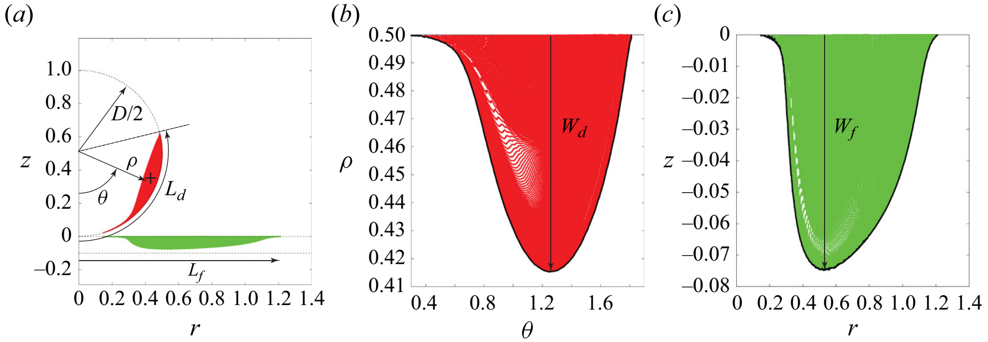

Figure 7. (*a*) Domains of fluid elements backtracked to $t = 0$ from $t = 0.9$ for $Re = 1000$, $We = 292$, $h = 0.1$. The dashed lines correspond to the drop surface (curved) and the film surface (upper flat) and the bottom boundary (lower flat). We extract the quantities L_d and W_d corresponding to the length and thickness of domains in the drop, and similarly L_f and W_f for the film. (*b*) Drop domain mapped to polar coordinates, where W_d is defined as the radial difference between the surface at $\rho = R$ and the tracer closest to the centre of the drop. (*c*) Film domain, where W_f is defined as the distance between the film surface and the deepest tracer. The black solid lines in (*b*,*c*) are the domain boundaries used to compute their volumes in the drop (V_d) and the film (V_f), factoring in the cylindrical geometry.

Rescaling W_d and V_d results in the data from all simulations collapsing onto a straight line on a log-log plot. Fits to a power law yield

$$W_d = 0.058h^{5/8}(L_d h^{-1/4})^{3.6} = 0.058h^{-0.28}L_d^{3.6} \sim h^{-0.28}(t - t_o)^{1.3}, \tag{3.2}$$

$$V_d = 0.071h(L_d h^{-1/4})^{5.1} = 0.071h^{-0.28}L_d^{5.1} \sim h^{-0.28}(t - t_o)^{1.8}, \tag{3.3}$$

where the time dependence follows from $L_d \sim (t - t_o)^{0.35}$. Rescaling W_f and V_f results in the data from all simulations collapsing onto a single curve, but the functional form is not readily apparent. These data give scaled forms

$$W_f = hF(L_d h^{-1/4}), \tag{3.4}$$

$$V_f = h^{7/4}G(L_d h^{-1/4}), \tag{3.5}$$

Here, L_f differs significantly from other domain parameters. As shown in figure 11, for thinner films $L_f \propto L_d$, but not for thicker films ($h \geq 0.1$). It is possible to collapse these data (see figure 11*c*), but the rescaling differs from that of other parameters. Considering the evolution of film domains in figure 6, one sees that they do not span the full depth of the film in thicker cases, suggesting that the solid substrate constrains the growth of the film domain for thinner films, and leads to qualitatively different growth in the two different limits.

The results for the fluid entrained into the bulb of the corolla, V_{frac} (ratio of the volume of liquid from the drop to the total volume of the bulb), were compared to those of Stumpf *et al.* (2022), who measured the secondary droplet composition. Since our axisymmetric simulation does not produce droplets, we approximated the composition of the droplet by measuring the composition of the bulb at the end of the corolla. We define the bulb to begin where the corolla develops a neck as the beginning of the liquid torus that would fragment into droplets. For $Re = 2042$, $We = 500$, $h = 0.2$ at $t = 0.5$, we observed $V_{frac} = 0.23$ inside the bulb, which is within the observed range in Stumpf *et al.* (2022, figure 14).

In addition to the power-law scaling of the characteristics of the domain in the drop, we find that the shape tends to a self-similar limit. Figure 12 plots the scaled domain

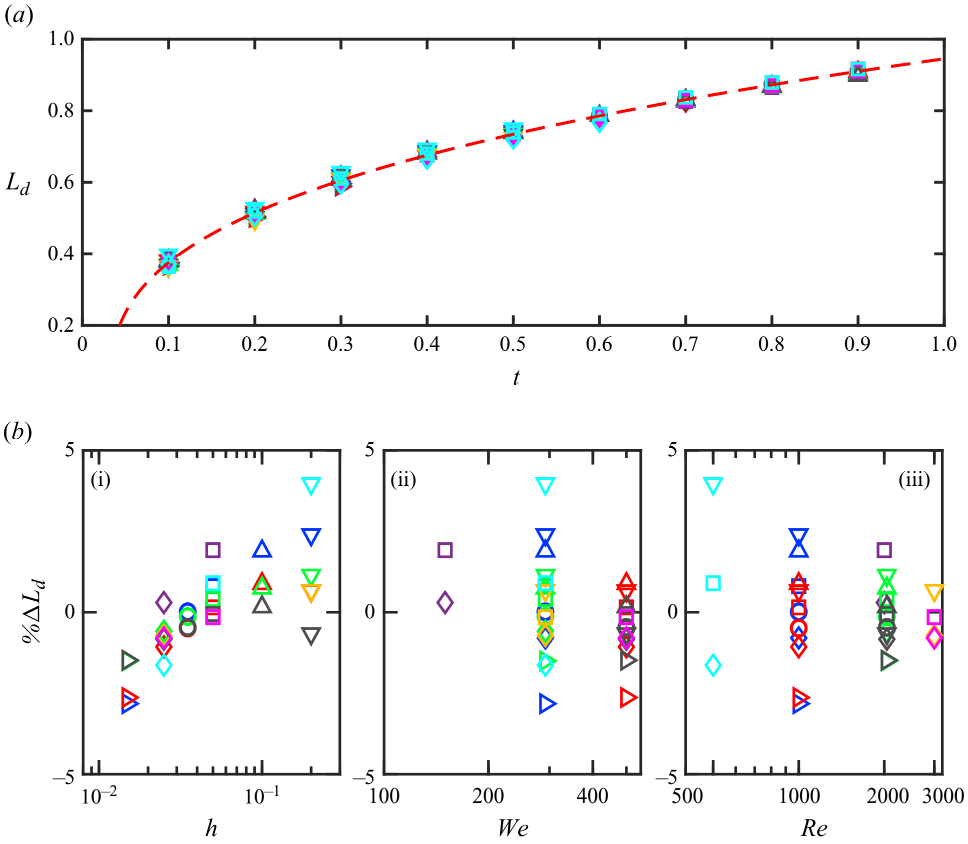

Figure 8. (*a*) Plot of L_d versus t for all 34 simulations. A fit to $B(t-t_o)^{\xi}$ is overlaid on the data (red dashed line), with $B = 0.96$, $t_o = 0.032$, $\xi = 0.35$. (*b*) Plots of $\%\Delta L_d \equiv (L_d/\overline{L_d} - 1)$ at $t = 0.3$ versus (i) h, (ii) We, (iii) Re. Combinations of Re and We are indicated by colour: green for $Re = 2042$, $We = 292$; red for $Re = 1000$, $We = 500$; blue for $Re = 1000$, $We = 292$; grey for $Re = 2042$, $We = 500$; yellow for $Re = 3000$, $We = 292$; fuchsia for $Re = 3000$, $We = 292$; cyan for $Re = 500$, $We = 292$; purple for $Re = 2000$, $We = 150$. Thickness h is indicated by symbols: ▹ for 0.015, ◇ for 0.025, ○ for 0.035, □ for 0.05, △ for 0.1, ▽ for 0.2. See supplementary material figure S4 available at https://doi.org/10.1017/jfm.2024.766.

boundaries, in polar coordinates as in figure 7, from all simulations with $h = 0.2$. We scale the raw shape (θ, ρ), which generally displays a single peak, by normalizing the peak height $(\rho \rightarrow (1-\rho)/W_d)$, zeroing the peak position $\theta \rightarrow 1 - \theta/\theta_{max}$, where θ_{max} is the angular position of the peak, and scaling the peak width by L_d^2. As shown in figures 12(*a*,*b*), the domain shape evolves towards the same shape irrespective of the Weber and Reynolds numbers in these scaled coordinates. We take the shape at $t = 0.9$ and $h = 0.2$ to be representative of the asymptotic form of the domain shape (see figure 12*c*), and compare this with the other depths in figure 13. These data suggest that all depths tend towards the same asymptotic form.

4. Summary and discussion

The corolla is composed of fluid that comes from both the drop and the pool. This is well-established fact corroborated by computations (e.g. Josserand & Zaleski 2003), experiments (e.g. W. van Hoeve, T. Segers, H. Kroes, D. Lohse & M. Versius, A splash

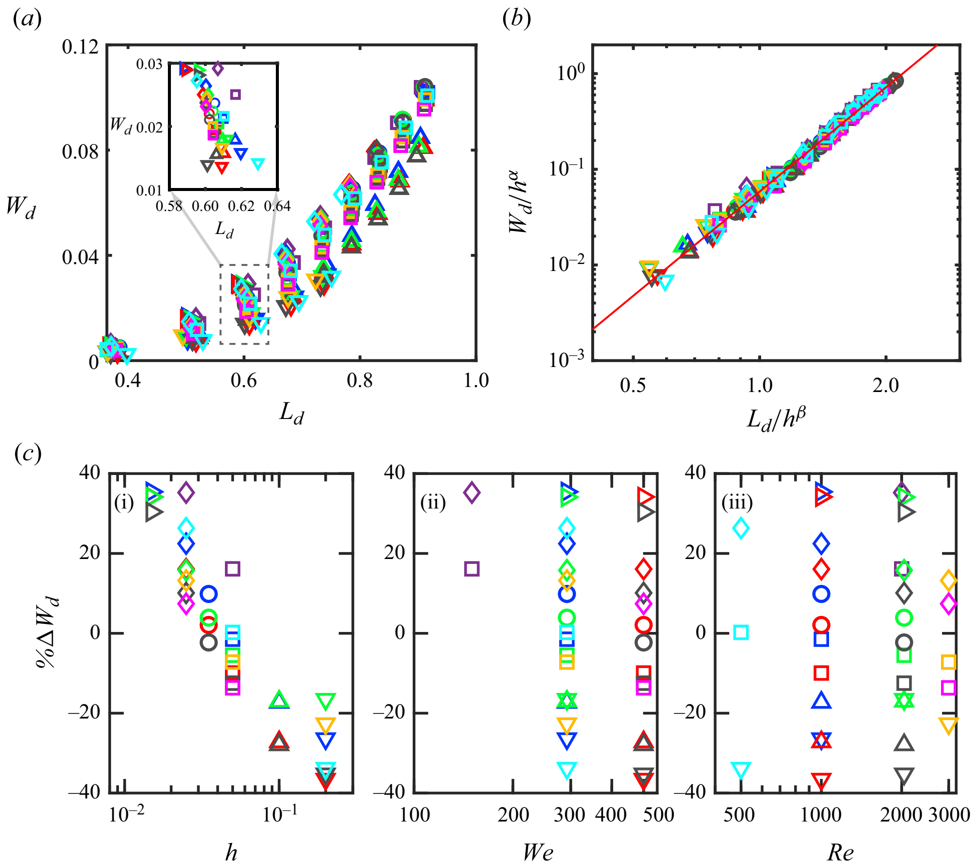

Figure 9. (*a*) Width versus length of drop domain, with the inset showing the same for $t = 0.3$ only. (*b*) Data in (*a*) scaled with h using the form of (3.1) with $\alpha = 5/8$ and $\beta = 1/4$. The red line is the best fit to a power law, yielding prefactor 0.059 and exponent 3.6. (*c*) Data at a fixed time (inset in *a*) plotted versus (i) h, (ii) We, (iii) Re. Symbols and colours are as in figure 8.

of red, private communication 2011; Versluis 2013), and theory (e.g. Cooker & Peregrine 1995; Howison *et al.* 2005). Recent work, particularly for the case where the drop and film are different fluids, has focused on quantifying the volumetric contribution from the drop versus that from the film (Fudge *et al.* 2023; Stumpf *et al.* 2022, 2023).

Using direct numerical simulations on an axisymmetric domain, we find that the fluid in the corolla at any moment of time produced by the impact of a spherical drop on a film comes from a thin layer on the drop's surface and a surface layer in the film that spans the film's full depth for thinner films. The novelty of our results is that they pinpoint the volume elements in each of the fluid bodies prior to impact from which the corolla is formed.

The shape of the domains that go on to form the corolla scales with the film thickness and is insensitive to the Weber and Reynolds numbers. A collapse of the data shows that the data for the drop domain are well modelled by a power law, and moreover, the boundary of the domain approaches a self-similar form. The contribution from the film also displays scaling with the thickness and insensitivity to the Reynolds and Weber numbers, but the

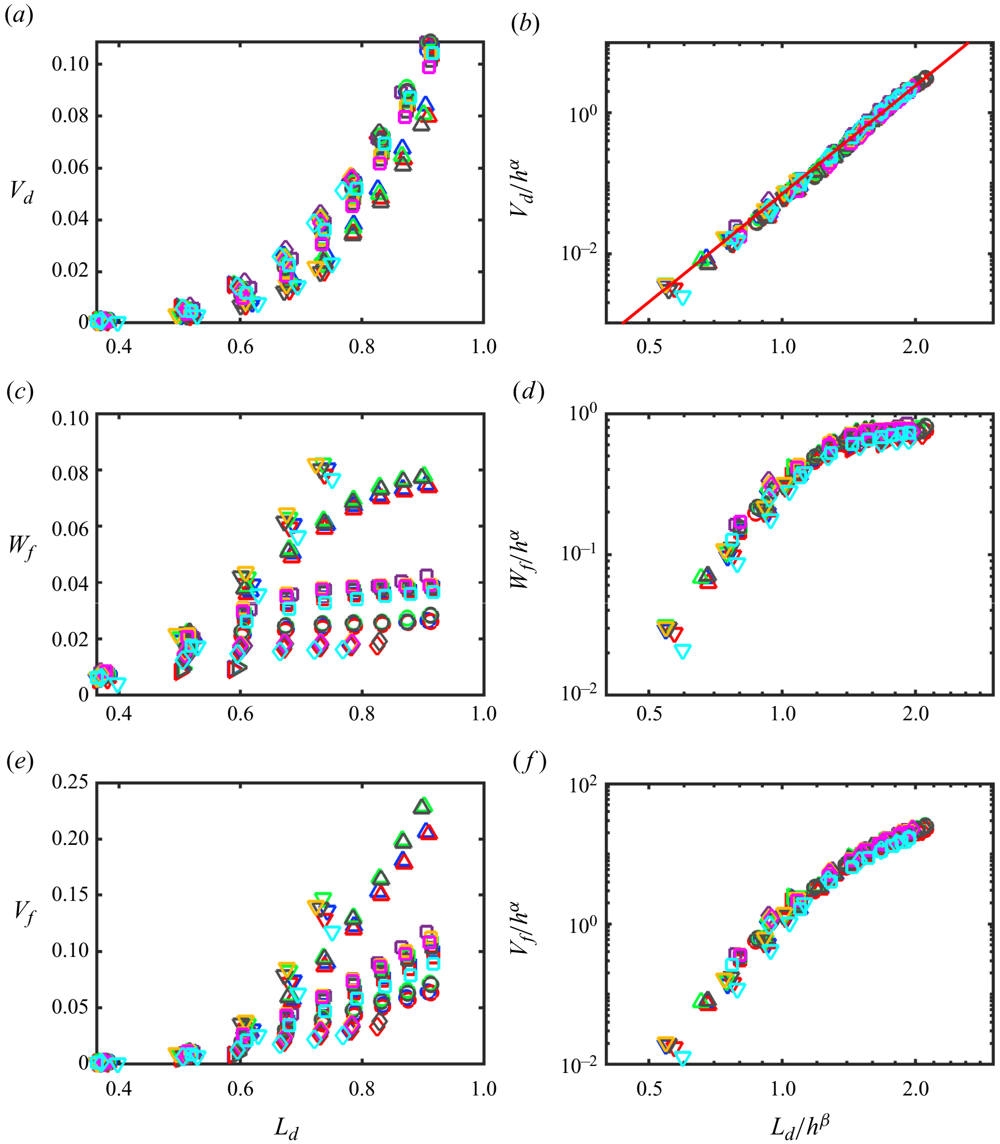

Figure 10. (a) Volume versus length of drop domain. (b) Same data as in (a) plotted with scaled variables with $\beta = 1/4$ and $\alpha = 1$. The red line is the best fit to a power law, yielding prefactor 0.071 and exponent 5.1. (c) Width of drop domain versus length of drop domain. (d) Same data as in (c) plotted with scaled variables with $\beta = 1/4$ and $\alpha = 1$. (e) Volume of drop domain versus length of drop domain. (f) Same data as in (e) plotted with scaled variables with $\beta = 1/4$ and $\alpha = 7/4$. Symbols and colours are as in figure 8.

collapsed data follow a more complex form that we attribute to the presence of a solid boundary beneath the film that limits the downward growth of the domain.

Our characterization would be useful for developing techniques to selectively disperse drop additives by seeding the parts of the drop that will later form the corolla. An advantage of this approach revealed by our study is that such a dispersal mechanism would be highly robust to variations of the Weber and Reynolds numbers.

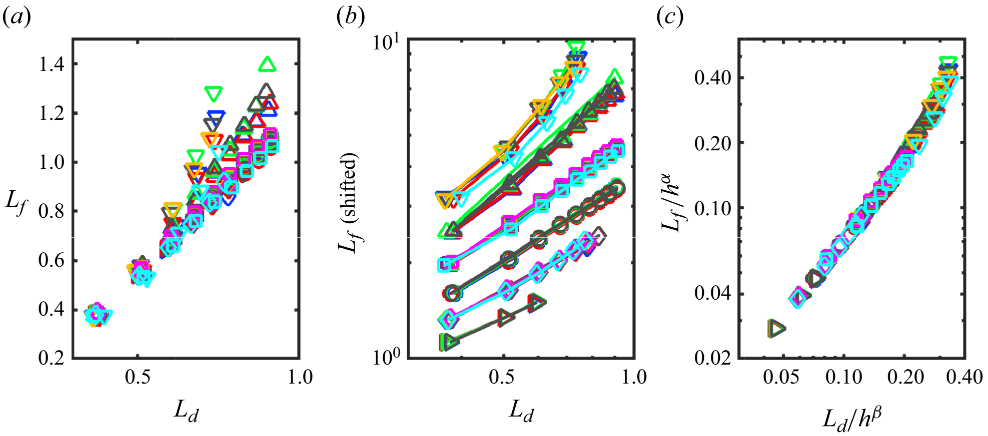

Figure 11. (*a*) Raw data for film length versus drop length. (*b*) Same data as in (*a*) on a log-log plot with different thicknesses shifted arbitrarily to better display their trends. (*c*) Scaling of data with $\alpha = -5/8$, $\beta = -1/2$. Symbols and colours are as in figure 8.

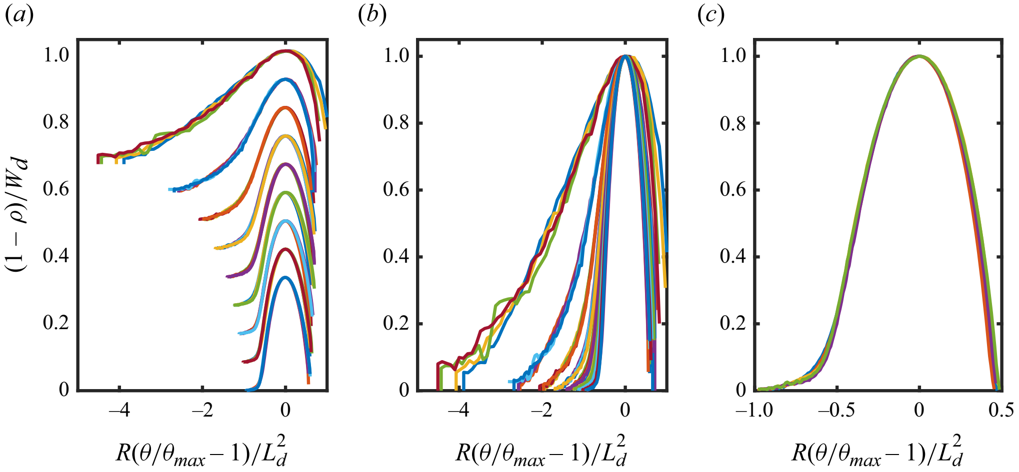

Figure 12. Profiles of the drop domains for $h = 0.2$ for all *Re*, *We*, and times shifted and scaled according to the formulas in the axis label so that their peaks coincide. (*a*) Profiles at different times shifted vertically for clarity with the topmost curve corresponding to $t = 0.1$, the next one down to $t = 0.2$, and so on up to $t = 0.9$. (*b*) Same data as in (*a*) without the vertical offset. (*c*) Data for all five profiles at $t = 0.9$.

The collapse of the scaled domains and their characteristics shows that their shape is predominantly governed by h, and the dependence on *We* and *Re* is all but negligible. In contrast, we observe large changes in the time evolution of the corolla's shape, and base thickness and speed with variations in the Reynolds and Weber numbers (see e.g. figure 14). Moreover, much of the literature on splashing revolves around correlating splashing with the Reynolds or Weber numbers, or various combination of these two. To give just two examples: Rioboo *et al.* (2003) showed that *We* sets a minimum threshold for the formation of a jet, and Yarin & Weiss (1995) showed that *We*/*Re* sets a threshold for splashing. Indeed, the most salient fact of drop impact is that speed matters: slow speeds lead to coalescence, and high speeds lead to splashing. The conundrum is how to reconcile

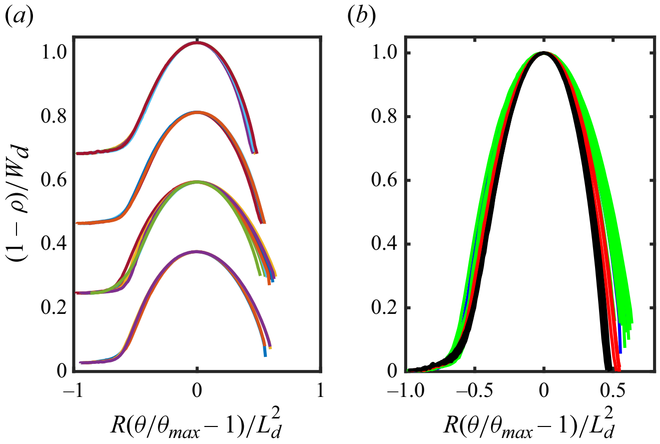

Figure 13. Profiles of the drop domains for all Re, We and h at $t = 0.9$ shifted and scaled according to the formulas in the axis label so that their peaks coincide. (*a*) Profiles for different film thicknesses shifted vertically for clarity, with topmost to bottommost corresponding respectively to $h = 0.2, 0.1, 0.05, 0.025$. (*b*) Same data as in (*a*) without the vertical offset.

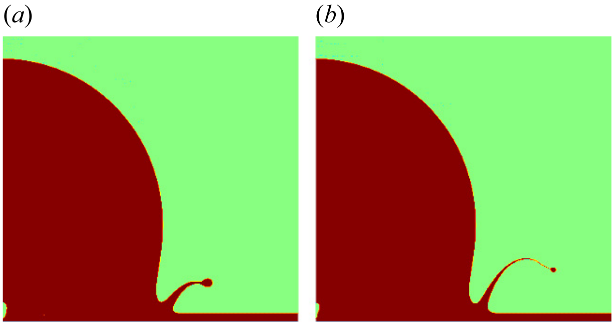

Figure 14. Comparison of interfaces for same depth $h = 0.025$ and time $t = 0.3$ for $Re = 1000$, $We = 292$ (*a*) and $Re = 3000$, $We = 500$ (*b*). More comparisons are shown in supplementary material figure S3.

changes in the time evolution of the corolla with Re and We, and the seemingly invariance to these values of the fluid elements that form the corolla.

The independence of L_d from all simulation parameters suggests looking for a physical mechanism in the geometric length scales intrinsic to an impact event. The penetration depth Ut/D (in unscaled units; just t in scaled units) is clearly not going to work as it varies as t, whereas $L_d \sim t^{0.35}$. The next candidate is L_g, the arc length of the submerged portion of the drop if the drop passed like a ghost through the film, i.e. the arc length on a circle crossed by a line a distance t from its apex:

$$L_g = \tfrac{1}{2}\arccos(1-2t). \tag{4.1}$$

As shown in figure 15(*a*), L_g provides a reasonable description of the data, especially at early times.

As an alternative avenue to explain our results, we considered the kinematic discontinuity theory of Yarin & Weiss (1995). The central result of the theory is that the radial distance at which the corolla emerges from the film scales as $h^{-1/4}$ but is otherwise independent of Re and We (Yarin & Weiss 1995; Rieber & Frohn 1999; Trujillo & Lee 2001; Roisman & Tropea 2002; Stumpf *et al.* 2023). The striking similarity to our

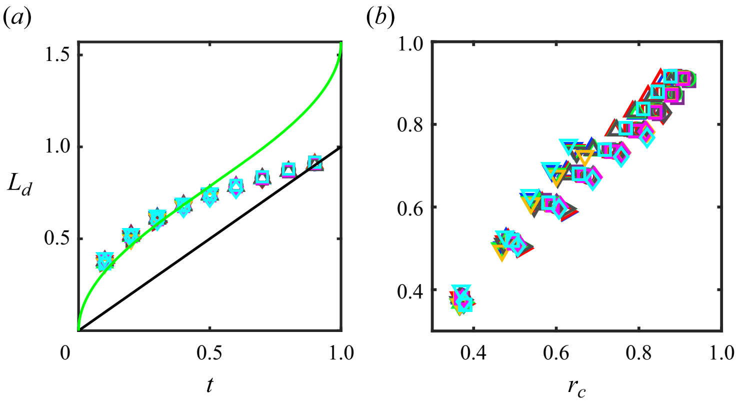

Figure 15. (*a*) Plot of L_d versus t. The green curved line is $L_g(t)$, and the black straight line is t. (*b*) Comparison of L_d and the crown radius r_c for assumption $r_c = r_A$. Symbols and colours are as in figure 8.

observed scaling $h^{-0.28}$ (see (3.3)), and *Re* and *We* independence, suggest that the theory may account for our results.

To examine this possibility, we tested the hypothesis that $L_d \propto r_c$, where r_c is the radial distance of the kinematic discontinuity (Yarin & Weiss 1995). Corollas always have a finite thickness, thus identifying r_c, which is a mathematical point in theory, is ambiguous. We tried two different schemes: (i) $r_c = r_A$ and (ii) $r_c = \frac{1}{2}(r_A + r_C)$, where r_A and r_C are the radial distances of points A and C in figure 4. Figure 15(*b*) shows that while $L_d \approx r_c$ (for scheme (i)), there is clearly a spread of the data that varies with the simulation parameters. The results were no better for scheme (ii). Thus the identification of L_d with r_c is not as good as with L_g. In the supplementary materials we show that the extension of the Yarin & Weiss (1995) theory in Stumpf *et al.* (2023) compares fairly well with the results of our simulations at the expense of introducing adjustable parameters that vary with the simulation parameters. Thus even though the extended theory works, it displays a dependence on Weber and Reynolds numbers that is at odds with our results.

Supplementary material. Supplementary material is available at https://doi.org/10.1017/jfm.2024.766.

Acknowledgements. We gratefully acknowledge discussions with X. Sodjavi.

Funding. R.D.D. acknowledges support for this work from NSF award no. 1802390.

Declaration of interests. The authors report no conflict of interest.

Data availability statement. Data supporting the findings of this study are available from the corresponding authors upon request.

Author ORCIDs.
Muhammad Osama https://orcid.org/0000-0002-2602-4380;
Robert D. Deegan https://orcid.org/0000-0002-9595-7395;
G. Gilou Agbaglah https://orcid.org/0000-0001-9669-9351.

REFERENCES

AFANADOR, A.R., ZALESKI, S., TRYGGVASON, G. & LU, J. 2021 Effect of topology changes on the breakup of a periodic liquid jet. *Comput. Fluids* **228**, 105059.

AGBAGLAH, G. & DEEGAN, R.D. 2014 Growth and instability of the liquid rim in the crown splash regime. *J. Fluid Mech.* **752**, 485–496.

AGBAGLAH, G., DELAUX, S., FUSTER, D., HOEPFFNER, J., JOSSERAND, C., POPINET, S., RAY, P., SCARDOVELLI, R. & ZALESKI, S. 2011 Parallel simulation of multiphase flows using octree adaptivity and the volume-of-fluid method. *C. R. Méc.* **339** (2–3), 194–207.

AGBAGLAH, G., THORAVAL, M.-J., THORODDSEN, S.T., ZHANG, L.V., FEZZAA, K. & DEEGAN, R.D. 2015 Drop impact into a deep pool: vortex shedding and jet formation. *J. Fluid Mech.* **764**, R1.

AKSOY, Y.T., ZHU, Y., ENEREN, P., KOOS, E. & VETRANO, M.R. 2021 The impact of nanofluids on droplet/spray cooling of a heated surface: a critical review. *Energies* **14** (1), 434–443.

AZIZ, S.D. & CHANDRA, S. 2000 Impact, recoil and splashing of molten metal droplets. *Intl J. Heat Mass Transfer* **43** (16), 2841–2857.

BARENBLATT, G.I. 2003 *Scaling*. Cambridge University Press.

BOUROUIBA, L. 2021 The fluid dynamics of disease transmission. *Annu. Rev. Fluid Mech.* **53**, 473–508.

BREITENBACH, J., ROISMAN, I.V. & TROPEA, C. 2018 From drop impact physics to spray cooling models: a critical review. *Exp. Fluids* **59** (3), 1–21.

CARSLAW, K.S., *et al.* 2013 Large contribution of natural aerosols to uncertainty in indirect forcing. *Nature* **503** (7474), 67.

CASTREJÓN-PITA, J.R., MUÑOZ-SÁNCHEZ, B.N., HUTCHINGS, I.M. & CASTREJÓN-PITA, A.A. 2016 Droplet impact onto moving liquids. *J. Fluid Mech.* **809**, 716–725.

COOKER, M.J. & PEREGRINE, D.H. 1995 Pressure-impulse theory for liquid impact problems. *J. Fluid Mech.* **297**, 193–214.

COSSALI, G.E., COGHE, A. & MARENGO, M. 1997 Impact of a single drop on a wetted solid surface. *Exp. Fluids* **22** (6), 463–472.

DAVIDSON, M.R. 2002 Spreading of an inviscid drop impacting on a liquid film. *Chem. Engng Sci.* **57** (17), 3639–3647.

DEEGAN, R.D., BRUNET, P. & EGGERS, J. 2008 Complexities of splashing. *Nonlinearity* **21** (1), C1–C11.

DUBITSKY, L., MCRAE, O. & BIRD, J.C. 2023 Enrichment of scavenged particles in jet drops determined by bubble size and particle position. *Phys. Rev. Lett.* **130** (5).

FUDGE, B.D., CIMPEANU, R., ANTKOWIAK, A., CASTREJÓN-PITA, J.R. & CASTREJÓN-PITA, A.A. 2023 Drop splashing after impact onto immiscible pools of different viscosities. *J. Colloid Interface Sci.* **641**, 585–594.

GAUTHIER, A., SYMON, S., CLANET, C. & QUERE, D. 2015 Water impacting on superhydrophobic macrotextures. *Nat. Commun.* **6**, 8001.

HARLOW, F.H. & SHANNON, J.P. 1967 Splash of a liquid drop. *J. Appl. Phys.* **38** (10), 3855.

HOWISON, S.D., OCKENDON, J.R., OLIVER, J.M., PURVIS, R. & SMITH, F.T. 2005 Droplet impact on a thin fluid layer. *J. Fluid Mech.* **542**, 1–23.

JOSSERAND, C., RAY, P. & ZALESKI, S. 2016 Droplet impact on a thin liquid film: anatomy of the splash. *J. Fluid Mech.* **802**, 775–805.

JOSSERAND, C. & THORODDSEN, S.T. 2016 Drop impact on a solid surface. *Annu. Rev. Fluid Mech.* **48**, 365–391.

JOSSERAND, C. & ZALESKI, S. 2003 Droplet splashing on a thin liquid film. *Phys. Fluids* **15** (6), 1650–1657.

KHOJASTEH, D., KAZEROONI, M., SALARIAN, S. & KAMALI, R. 2016 Droplet impact on superhydrophobic surfaces: a review of recent developments. *J. Ind. Engng Chem.* **42**, 1–14.

TAO LI, H., LI, J., ZONG, Z. & CHEN, Z. 2014 Numerical studies on sloshing in rectangular tanks using a tree-based adaptive solver and experimental validation. *Ocean Engng* **82**, 20–31.

LIANG, G. & MUDAWAR, I. 2016 Review of mass and momentum interactions during drop impact on a liquid film. *Intl J. Heat Mass Transfer* **101**, 577–599.

LIANG, G. & MUDAWAR, I. 2017 Review of drop impact on heated walls. *Intl J. Heat Mass Transfer* **106**, 103–126.

LING, Y., FULLANA, J.-M., POPINET, S. & JOSSERAND, C. 2016 Droplet migration in a Hele-Shaw microchannel: effect of the lubrication film on the droplet dynamics. *Phys. Fluids* **28**, 062001.

LOHSE, D. 2022 Fundamental fluid dynamics challenges in inkjet printing. *Annu. Rev. Fluid Mech.* **54**, 349–382.

MARENGO, M., ANTONINI, C., ROISMAN, I.V. & TROPEA, C. 2011 Drop collisions with simple and complex surfaces. *Curr. Opin. Colloid Interface Sci.* **16** (4), 292–302.

MOREIRA, A.L.N., MOITA, A.S. & PANAO, M.R. 2010 Advances and challenges in explaining fuel spray impingement: how much of single droplet impact research is useful? *Prog. Energy Combust. Sci.* **36** (5), 554–580.

MUNDO, C., SOMMERFELD, M. & TROPEA, C. 1995 Droplet–wall collisions: experimental studies of the deformation and breakup process. *Intl J. Multiphase Flow* **21** (2), 151–173.

OSAMA, M., DENG, P., THORAVAL, M.-J. & AGBAGLAH, G.G. 2022 Dynamics of finite-size air filaments in a static liquid. *Phys. Fluids* **34** (6), 062106.

PEREGRINE, D.H. 1981 The fascination of fluid-mechanics. *J. Fluid Mech.* **106**, 59–80.

POPINET, S. 2003 Gerris: a tree-based adaptive solver for the incompressible Euler equations in complex geometries. *J. Comput. Phys.* **190**, 572–600.

POPINET, S. 2009 An accurate adaptive solver for surface-tension-driven interfacial flows. *J. Comput. Phys.* **228**, 5838–5866.

POPINET, S. 2018 Basilisk, a free-software program for the solution of partial differential equations on adaptive Cartesian meshes. http://basilisk.fr.

REIN, M. 1993 Phenomena of liquid drop impact on solid and liquid surfaces. *Fluid Dyn. Res.* **12** (2), 61–93.

RIEBER, M. & FROHN, A. 1999 A numerical study on the mechanism of splashing. *Intl J. Heat Fluid Flow* **20** (5), 455–461.

RIOBOO, R., BAUTHIER, C., CONTI, J., VOUE, M. & DE CONINCK, J. 2003 Experimental investigation of splash and crown formation during single drop impact on wetted surfaces. *Exp. Fluids* **35**, 648–652.

ROISMAN, I.V. & TROPEA, C. 2002 Impact of a drop onto a wetted wall: description of crown formation and propagation. *J. Fluid Mech.* **472**, 373–397.

STUMPF, B., ROISMAN, I.V., YARIN, A.L. & TROPEA, C. 2023 Drop impact onto a substrate wetted by another liquid: corona detachment from the wall film. *J. Fluid Mech.* **956**, A10.

STUMPF, B., RUESCH, J.H., ROISMAN, I.V., TROPEA, C. & HUSSONG, J. 2022 An imaging technique for determining the volume fraction of two-component droplets of immiscible fluids. *Exp. Fluids* **63**, 114.

THORAVAL, M.-J., TAKEHARA, K., ETOH, T.G., POPINET, S., RAY, P., JOSSERAND, C., ZALESKI, S. & THORODDSEN, S.T. 2012 von Kármán vortex street within an impacting drop. *Phys. Rev. Lett.* **108** (26), 264506.

THORAVAL, M.-J., TAKEHARA, K., ETOH, T.G. & THORODDSEN, S.T. 2013 Drop impact entrapment of bubble rings. *J. Fluid Mech.* **724**, 234–258.

THORODDSEN, S.T. 2002 The ejecta sheet generated by the impact of a drop. *J. Fluid Mech.* **451**, 373–381.

TRAN, T., STAAT, H.J.J., PROSPERETTI, A., SUN, C. & LOHSE, D. 2012 Drop impact on superheated surfaces. *Phys. Rev. Lett.* **108** (3), 036101.

TRUJILLO, M.F. & LEE, C.F. 2001 Modeling crown formation due to the splashing of a droplet. *Phys. Fluids* **13** (9), 2503–2516.

VAN HOOFT, J.A., POPINET, S., VAN HEERWAARDEN, C.C., VAN DER LINDEN, S.J.A., DE ROODE, S.R. & VAN DE WIEL, B.J.H. 2018 Towards adaptive grids for atmospheric boundary-layer simulations. *Boundary-Layer Meteorol.* **167** (3), 421–443.

VAN DER VEEN, R.C.A., TUAN, T., LOHSE, D. & SUN, C. 2012 Direct measurements of air layer profiles under impacting droplets using high-speed color interferometry. *Phys. Rev.* E **85**, 026315.

VERSLUIS, M. 2013 High-speed imaging in fluids. *Exp. Fluids* **54**, 1–35.

VILLERMAUX, E. 2007 Fragmentation. *Annu. Rev. Fluid Mech.* **39**, 419–446.

VISSER, C.W., FROMMHOLD, P.E., WILDEMAN, S., METTIN, R., LOHSE, D. & SUN, C. 2015 Dynamics of high-speed micro-drop impact: numerical simulations and experiments at frame-to-frame times below 100 ns. *Soft Matt.* **11** (9), 1708–1722.

WANG, A.-B. & CHEN, C.-C. 2000 Splashing impact of a single drop onto very thin liquid films. *Phys. Fluids* **12** (9), 2155–2158.

WEISS, D.A. & YARIN, A.L. 1999 Single drop impact onto liquid films: neck distortion, jetting, tiny bubble entrainment, and crown formation. *J. Fluid Mech.* **385**, 229–254.

WORTHINGTON, A.M. & COLE, R.S. 1897 Impact with a liquid surface, studied by the aid of instantaneous photography. *Phil. Trans. R. Soc. Lond.* A **189**, 137–148.

XU, L. 2007 Liquid drop splashing on smooth, rough, and textured surfaces. *Phys. Rev.* E **75**, 056316.

YARIN, A.L. 2006 Drop impact dynamics: splashing, spreading, receding, bouncing. *Annu. Rev. Fluid Mech.* **38**, 159–192.

YARIN, A.L. & WEISS, D.A. 1995 Impact of drops on solid-surfaces – self-similar capillary waves, and splashing as a new type of kinematic discontinuity. *J. Fluid Mech.* **283**, 141–173.

ZHANG, L.V., TOOLE, J., FEZZAA, K. & DEEGAN, R.D. 2012 Evolution of the ejecta sheet from the impact of a drop with a deep pool. *J. Fluid Mech.* **690**, 5.

ZHOU, Y., *et al.* 2021 Rayleigh–Taylor and Richtmyer–Meshkov instabilities: a journey through scales. *Physica* D **423**, 132838.